Widefield Parametric Polar Format Algorithm for Spotlight SAR Imaging

Zhichao Meng, Lei Zhang, *Member, IEEE*, and Lili Chen

***Abstract*—For widefield synthetic aperture radar (SAR) imaging, range-dependent motion errors and range curvature are the main obstacle for range cell migration correction (RCMC) and azimuth focusing. The parametric polar format algorithm (PPFA) can handle the range-dependent motion errors after RCMC, but the nonsystem range cell migration is ignored. Furthermore, the residual range curvature is neglected, causing the undesired range cell migration. In this article, a novel widefield PPFA is developed for widefield spotlight SAR imaging. A precise range-compressed domain motion compensation algorithm is introduced for the range-dependent motion errors. It can precisely compensate for the range-dependent motion errors before RCMC. After RCMC, an accurate range curvature correction algorithm is carried out, accelerated by the scaling Fourier transform. Based on these improvements, an azimuth wavenumber resampling integrating azimuth-variant phase error compensation is implemented to achieve well-focused images. Finally, extensive simulated and real-measured SAR data have validated the algorithm's effectiveness.**

***Index Terms*—Nonsystem range cell migration (NsRCM), parametric polar format algorithm (PPFA), range-compressed domain motion compensation (RC-MOCO), range-dependent motion errors, synthetic aperture radar (SAR).**

I. Introduction

SYNTHETIC aperture radar (SAR) [1], [2], [3] is an advanced microwave remote sensing device. It is able to achieve Earth observation in all-day and all-weather. Its high-resolution flexibility and wide-area observation capability have attracted worldwide attention. With the development of Earth observation missions, wider swaths have become essential features of modern SAR [4], [5], [6], [7]. As a result, the development of accurate imaging and motion compensation (MOCO) algorithms for widefield SAR has become an urgent issue.

Current popular SAR algorithms can be roughly sorted into three classes, i.e., time domain algorithm [8], [9], [10], [11], [12], [13], [14], [15], [16], frequency domain algorithm [17], [18], [19], [20], [21], [22], [23], [24], [25], [26], [27], and time-frequency hybrid algorithm [28], [29], [30], [31], [32]. The classical time-domain algorithms, such as the fast back-projection (BP) algorithm [9], [10], the fast factorized BP algorithm [11], [12], [13], and the Cartesian factorized BP algorithm [14], [15], [16], are all improved algorithms based on the BP algorithm [8]. These algorithms perform accurate two-dimensional pulse compression of echoes by calculating the phase history of the imaging grid point by point. They are able to overcome various motion errors to generate high-resolution imaging results, but the high computational complexity limits their application. The typical representatives of the frequency domain algorithm are range Doppler (RD) algorithm [17], [18], [19], [20], chirp scaling (CS) algorithm [21], [22], [23], [24], and range migration algorithm (RMA) [25], [26], [27]. Among them, the RD and CS algorithms achieve uniform processing by low-order approximation of the echo signal, while the RMA algorithm achieves batch processing of the echo signal by interpolating the exact two-dimensional wavenumber spectrum. To compensate for motion errors, they often need to be combined with the "two-step" MOCO algorithm [28], [29], [30]. However, for spatial-variant motion errors, the more complex MOCO algorithms or the lower order signal expressions have to be used, increasing the complexity and limiting the algorithm's accuracy. In contrast to the previous two, the time-frequency hybrid algorithms achieve fast two-dimension focusing of echoes by alternating processing in the time and frequency domains. The polar format algorithm (PFA) [31], [32], [33] and the parametric polar format algorithm (PPFA) [34], [35] are two prime representatives of this class. Since the SAR imagery formed by these algorithms is in the Doppler domain and the signal before azimuth focusing is consistent with the actual slow-time, they can be easily combined with various autofocusing algorithms [36], [37]. As a result, they are frequently used in spotlight SAR imaging missions.

As previously stated, PFA achieves the two-dimension focusing by alternating interpolation in the time and frequency domains. The planar wavefront hypothesis [38], [39], [40], which limits the size of the imaging scene, is the only assumption in PFA. In other words, the imagery can be well-focused if the scenario is small enough. For the widefield SAR task, a common method is image block division. However, the spatial-variant motion error compensation is complicated because the original interpolation operation does not adequately account for these spatial-variant motion errors. As a result, some complex postprocessing algorithms [41], [42] are required,

Manuscript received 30 March 2023; revised 15 May 2023; accepted 14 June 2023. Date of publication 26 June 2023; date of current version 9 August 2023. This work was supported in part by the introduced innovative R&D team project of "The Pearl River Talent Recruitment Program" under Grant 2019ZT08X751, in part by the Aeronautical Science Foundation of China under Grant 2019200M1001, and in part by the Guangdong Key Laboratory of Advanced IntelliSense Technology under Grant 2019B111101001. *(Corresponding authors: Lei Zhang; Lili Chen.)*

Zhichao Meng and Lei Zhang are with the School of Electronics and Communication Engineering, Sun Yat-sen University, Shenzhen 518107, China (e-mail: m1395378188@163.com; zhanglei57@mail.sysu.edu.cn).

Lili Chen is with the Artificial Intelligence Research Center, National Innovation Institute of Defense Technology, Beijing 100071, China (e-mail: chenlili8209@nudt.edu.cn).

Digital Object Identifier 10.1109/JSTARS.2023.3289216

significantly increasing the computation burden. To handle this problem, the PPFA [31] is developed. PPFA thoroughly considers the effect of spatial-variant motion errors and uses the platform's motion errors as the parameters of interpolation operation to achieve accurate spatial-variant motion error compensation while resampling the azimuthal wavenumber. However, on the one hand, the original PPFA considers the range-dependent motion errors so minor that the impact on the signal envelope can be ignored before the range cell migration correction (RCMC). On the other hand, the original PPFA ignores the residual range curvature after range walk correction to simplify the RCMC procedure. These assumptions are reasonable in low-resolution narrow-swath SAR but significantly decrease the effective slant-range focusing depth in high-resolution and widefield SAR.

To realize the widefield spotlight SAR imaging, a widefield parametric polar format algorithm (WPPFA) is proposed in this article. First, a novel range-compressed domain MOCO (RC-MOCO) algorithm for spotlight SAR is developed to compensate precisely for the range-dependent motion errors. It paves the way for precise RCMC and, ultimately, azimuth focusing. The accurate mathematical model of residual range curvature is investigated based on the signal whose range-dependent motion errors have been eliminated. According to the model, a range curvature correction (RCC) algorithm is introduced. We improve its efficiency while maintaining accuracy by scaling the Fourier transform (SFT). Based on these advancements, an azimuth wavenumber resampling integrated azimuth-variant phase error compensation is utilized to focus the azimuthal signal.

The rest of this article is organized as follows. Section II describes the signal model of high-resolution and widefield SAR and profoundly analyzes the existing problems in PPFA. In Section III, the proposed algorithm is introduced in detail. The extensive experiments with simulated and real-measured airborne SAR data are shown in Section IV. Finally, Section V concludes this article.

II. Mathmatical Model of PPFA

This section introduces the fundamental mathematical model of SAR echo and the PPFA algorithm so that the subsequent enhanced PPFA can be easily understood. The geometry of spotlight SAR imaging is shown in Fig. 1. The platform flies on the height H with a constant velocity v in the ideal condition. The black dashed line is the ideal trajectory, and the red dashed curve is the actual trajectory. At a specific moment, the nominal antenna phase center (APC) is $A(X,0,H)$, while the actual APC is $A'(X+\Delta X,\Delta Y,H+\Delta Z)$ due to atmospheric turbulence. The ΔX, ΔY, and ΔZ are the three-axis deviations, respectively.

According to the geometry model, the actual range history $R(t,\Delta;\theta_\mathrm{p},r_\mathrm{p})$ from the actual APC $A'(X+\Delta X,\Delta Y,H+\Delta Z)$ to the point $p_\mathrm{p}(r_\mathrm{p},\theta_\mathrm{p})$ is represented by

$$R\left(X,\Delta,\theta_\mathrm{p},r_\mathrm{p}\right) = \sqrt{\left(X+\Delta X-x_\mathrm{p}\right)^2+\left(\Delta Y-y_\mathrm{p}\right)^2+\left(H+\Delta Z\right)^2} \quad (1)$$

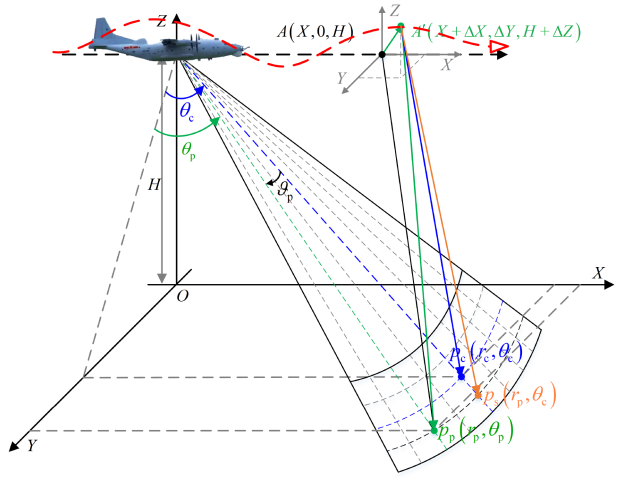

Fig. 1. SAR imaging geometry with polar coordinate.

where, $X=vt$, t is slow time variable, and Δ donates the three-axis motion errors. In addition

$$x_\mathrm{p} = r_\mathrm{p}\sin\theta_\mathrm{p} \quad (2a)$$

$$y_\mathrm{p} = \sqrt{\left(r_\mathrm{p}\cos\theta_\mathrm{p}\right)^2 - H^2}. \quad (2b)$$

Furthermore, when the SAR system transmits a linear frequency modulate signal with centroid frequency f_c and bandwidth B, the base-band signal in range wavenumber domain can be given by

$$S_0\left(k_\mathrm{r},X,\Delta,\theta_\mathrm{p}\right) = \exp\left[-j\left(k_\mathrm{r}+k_\mathrm{rc}\right)R\left(X,\Delta,\theta_\mathrm{p},r_\mathrm{p}\right)\right] \quad (3)$$

where, $k_\mathrm{r}=4\pi f_\mathrm{r}/c$ is the range wavenumber, $f_\mathrm{r}\in[-B/2\ ,B/2\ ]$, and $k_\mathrm{rc}=4\pi f_\mathrm{c}/c$. Similarly, the instantaneous range from the APC to the reference point $p_\mathrm{c}(r_\mathrm{c},\theta_\mathrm{c})$ is given by

$$R\left(X,\Delta,\theta_\mathrm{c},r_\mathrm{c}\right) = \sqrt{\left(X+\Delta X-x_\mathrm{c}\right)^2+\left(\Delta Y-y_\mathrm{c}\right)^2+\left(H+\Delta Z\right)^2}. \quad (4)$$

In the original PPFA, the spatial-invariant MOCO and azimuth dechirp procedures are implemented by multiplying the reference function H_1

$$H_1\left(k_\mathrm{r},X,\Delta\right) = \exp\left[jk_\mathrm{r}\cdot R\left(X,\Delta,\theta_\mathrm{c},r_\mathrm{c}\right)\right]. \quad (5)$$

Then, the dechirped signal is given by

$$\begin{aligned} S_1\left(k_\mathrm{r},X,\Delta,\theta_\mathrm{p}\right) &= \exp\left[-jk_\mathrm{r}\cdot\left(R\left(X,\Delta,\theta_\mathrm{p},r_\mathrm{p}\right)-R\left(X,\Delta,\theta_\mathrm{c},r_\mathrm{c}\right)\right)\right] \\ &= \exp\left(-jk_\mathrm{r}\cdot\Delta R\left(X,\Delta,\theta_\mathrm{p},r_\mathrm{p}\right)\right) \end{aligned} \quad (6)$$

where, the instantaneous differential range $\Delta R(X,\Delta,\theta_\mathrm{p},r_\mathrm{p})$ is

$$\Delta R\left(X,\Delta,\theta_\mathrm{p},r_\mathrm{p}\right) = R\left(X,\Delta,\theta_\mathrm{p},r_\mathrm{p}\right) - R\left(X,\Delta,\theta_\mathrm{c},r_\mathrm{c}\right). \quad (7)$$

After performing Taylor series expansion at $\theta_\mathrm{p}=\theta_\mathrm{c}$ and neglecting the second-order and high-order terms, the (7) is rewritten

as

$$\Delta R\left(X,\Delta,\vartheta_{\mathrm{p}},r_{\mathrm{p}}\right) = \alpha_0\left(X,\Delta,\theta_{\mathrm{c}},r_{\mathrm{p}}\right)+\alpha_1\left(X,\Delta,\theta_{\mathrm{c}},r_{\mathrm{p}}\right)\cdot\vartheta_{\mathrm{p}}+o\left(\vartheta_{\mathrm{p}}\right) \quad (8)$$

where, $\vartheta_{\mathrm{p}}=\theta_{\mathrm{p}}-\theta_{\mathrm{c}}$ is difference azimuth angle variable and the zero-order term $\alpha_0(X,\Delta,\theta_{\mathrm{c}},r_{\mathrm{p}})=R(X,\Delta,\theta_{\mathrm{c}},r_{\mathrm{p}})-R(X,\Delta,\theta_{\mathrm{c}},r_{\mathrm{c}})$ contains the range-dependent residual range curvature and motion errors. In addition, the second term is given by

$$\alpha_1\left(X,\Delta,\theta_{\mathrm{c}},r_{\mathrm{p}}\right) = \frac{-r_{\mathrm{p}}\cos\theta_{\mathrm{c}}}{R\left(X,\Delta,\theta_{\mathrm{c}},r_{\mathrm{p}}\right)}\left(X+\Delta X-\Delta Y\cdot\tan\varphi_{\mathrm{pc}}\right) \quad (9)$$

where, $\tan\varphi_{\mathrm{pc}}=x_{\mathrm{pc}}/y_{\mathrm{pc}}$, and

$$x_{\mathrm{pc}}=r_{\mathrm{p}}\sin\theta_{\mathrm{c}} \quad (10a)$$

$$y_{\mathrm{pc}}=\sqrt{\left(r_{\mathrm{p}}\cos\theta_{\mathrm{c}}\right)^2-H^2}. \quad (10b)$$

From (9), one can see that when $\Delta X,\Delta Y\ll r_{\mathrm{c}}$, the one-order term coefficient $\alpha_1(X,\Delta,\theta_{\mathrm{c}},r_{\mathrm{p}})$ can be approximated by a linear function

$$\alpha_1\left(X,\Delta,\theta_{\mathrm{c}},r_{\mathrm{p}}\right)\approx -X\cdot\cos\theta_{\mathrm{c}}. \quad (11)$$

In addition, when the condition $|\frac{r_{\mathrm{p}}-r_{\mathrm{c}}}{r_{\mathrm{c}}}|\le 1$ is hold, the impact on the envelop of $S_1(k_r,X,\Delta,\theta_{\mathrm{p}})$ bringing by $\alpha_0(X,\Delta,\theta_{\mathrm{c}},r_{\mathrm{p}})$ and the high-order term $o(\vartheta_{\mathrm{p}})$ can be neglected. As a result, PPFA performs the RCMC by keystone transform algorithm (KTA) [43], which is equivalent to a variable substitution processing

$$k_{\mathrm{rc}}\cdot\tilde{X}=\left(k_{\mathrm{r}}+k_{\mathrm{rc}}\right)\cdot X\Leftrightarrow\tilde{X}=\frac{k_{\mathrm{r}}+k_{\mathrm{rc}}}{k_{\mathrm{rc}}}X=\gamma_k\cdot X. \quad (12)$$

One can see that KTA achieves the slow time scaling transform with the scaling factor γ_k. To simplify, the new slow time variable $\tilde{X}$ still replaced by X after KTA processing. The decoupled signal in 2-D time domain is given by

$$S_2\left(X,\Delta,\vartheta_{\mathrm{p}},r_{\mathrm{p}}\right)=\mathrm{sinc}\left(r-\Delta r_{\mathrm{pc}}\right) \cdot\exp\left[-jk_{\mathrm{rc}}\left(\alpha_0\left(X,\Delta,\theta_{\mathrm{c}},r_{\mathrm{p}}\right)+\alpha_1\left(X,\Delta,\theta_{\mathrm{c}},r_{\mathrm{p}}\right)\vartheta_{\mathrm{p}}\right)\right] \quad (13)$$

where, the $\Delta r_{\mathrm{pc}}=r_{\mathrm{p}}-r_{\mathrm{c}}$ is the range difference between target $p_{\mathrm{p}}(r_{\mathrm{p}},\theta_{\mathrm{p}})$ and reference point $p_{\mathrm{c}}(r_{\mathrm{c}},\theta_{\mathrm{c}})$. In the following processing of PPFA, the range-dependent range curvature phase and motion error phase are compensated by the reference function H_2:

$$H_2\left(X,\Delta,r_{\mathrm{p}}\right)=\exp\left[jk_{\mathrm{rc}}\cdot\alpha_0\left(X,\Delta,\theta_{\mathrm{c}},r_{\mathrm{p}}\right)\right]. \quad (14)$$

After phase compensation, the (13) is rewritten as

$$S_3\left(X,\Delta,\vartheta_{\mathrm{p}},r_{\mathrm{p}}\right) =\mathrm{sinc}\left(r-\Delta r_{\mathrm{pc}}\right)\cdot\exp\left(-jk_{\mathrm{rc}}\alpha_1\left(X,\Delta,\theta_{\mathrm{c}},r_{\mathrm{p}}\right)\cdot\vartheta_{\mathrm{p}}\right). \quad (15)$$

Moreover, the azimuth angle wavenumber is defined as

$$k_{\vartheta}\left(X,\Delta,r_{\mathrm{p}}\right)=k_{\mathrm{rc}}\cdot\alpha_1\left(X,\Delta,\theta_{\mathrm{c}},r_{\mathrm{p}}\right). \quad (16)$$

The (15) rewritten as

$$S_3\left(X,\Delta,\vartheta_{\mathrm{p}},r_{\mathrm{p}}\right) =\mathrm{sinc}\left(r-\Delta r_{\mathrm{pc}}\right)\cdot\exp\left[-jk_{\vartheta}\left(X,\Delta,r_{\mathrm{p}}\right)\cdot\vartheta_{\mathrm{p}}\right]. \quad (17)$$

One can see from (17), $S_3(X,\Delta,\vartheta_{\mathrm{p}},r_{\mathrm{p}})$ is a single-frequency signal with the center frequency $\frac{\vartheta_{\mathrm{p}}}{2\pi}$ in the azimuth angle wavenumber domain. For this reason, the well-focused SAR imagery can be formed by inverse fast Fourier transform (IFFT) operation along azimuth angle wavenumber axis. However, the azimuth angle wavenumber $k_{\vartheta}(X,\Delta,r_{\mathrm{p}})$ has the nonuniform sample interval due to the nonlinear function $\alpha_1(X,\Delta,\theta_{\mathrm{c}},r_{\mathrm{p}})$, precluding well-focused SAR imagery formation. Therefore, an azimuthal uniform sampling operation for $k_{\vartheta}(X,\Delta,r_{\mathrm{p}})$ is required. For simplify, we refer to the uniformly sampled $k_{\vartheta}(X,\Delta,r_{\mathrm{p}})$ as k_{ϑ}. Based on this, (17) becomes

$$S_3\left(k_{\vartheta},\vartheta_{\mathrm{p}}\right)=\mathrm{sinc}\left(r-\Delta r_{\mathrm{pc}}\right)\cdot\exp\left[-jk_{\vartheta}\cdot\vartheta_{\mathrm{p}}\right]. \quad (18)$$

After resampling $k_{\vartheta}(X,\Delta,r_{\mathrm{p}})$ at equal intervals for every range cell r, the image $I(\Delta,\vartheta,r)$ in polar coordinate can be obtained by IFFT along azimuth angle wavenumber axis, i.e.,

$$I\left(\Delta,\vartheta,r\right)=\mathrm{IFFT}_{k_{\vartheta}}\left[S_3\left(k_{\vartheta},\vartheta_{\mathrm{p}}\right)\right] =\mathrm{sinc}\left(r-\Delta r_{\mathrm{pc}}\right)\cdot\mathrm{sinc}\left(\vartheta-\vartheta_{\mathrm{p}}\right). \quad (19)$$

From (15)–(19), it is clear that the nonuniform azimuth angle wavenumber variable $k_{\vartheta}(X,\Delta,r_{\mathrm{p}})$ contains three-axis motion errors, resulting in the defocused SAR imagery. Therefore, the azimuth resampling operation not only promises a fast azimuth focusing by IFFT but achieves azimuth-variant MOCO. Compared with conventional subaperture division and frequency division algorithms, PPFA can perform azimuth-variant MOCO precisely and efficiently. Since the resampling takes motion errors as parameters, it is called parametric azimuth resampling.

III. Widefield PPFA

Section II shows two vital hypotheses in PPFA. First, the nonsystem range cell migration (NsRCM) caused by range-dependent motion errors is ignored before the RCMC. The second is that the residual range-dependent range curvature is neglected when correcting range cell walk. These approximations can always be guaranteed in narrow-field SAR imaging. However, the severe NsRCM and range cell curvature will become nonnegligible for widefield spotlight SAR imaging, resulting in SAR image degradation. This section proposes a WPPFA algorithm to achieve high-resolution widefield spotlight SAR imaging. First, a novel RC-MOCO algorithm is developed to eliminate the NsRCM and azimuth phase errors caused by range-dependent motion errors. Following range walk correction, an RCC approach is introduced to correct the residual range curvature. And SFT is embedded into RCC to improve efficiency. Finally, based on these improvements, the azimuth wavenumber resampling is used to focus the azimuth signal.

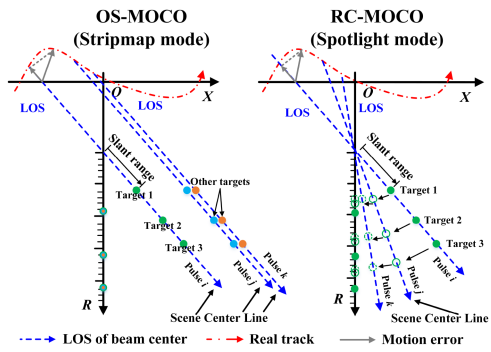

Fig. 2. Distinctions between OS-MOCO and RC-MOCO.

A. Precise RC-MOCO

From (6)–(8), we can see that the residual zero-order term $\alpha_0(X, \Delta, \theta_c, r_p)$, including range curvature and range-dependent motion errors, do not be considered when KTA is executed. In this section, the range-dependent motion errors are first considered. We rewrite it as

$$\alpha_0\left(X, \Delta, \theta_c, r_p\right) = \tilde{\alpha}_0\left(X, \theta_c, r_p\right) + \mathrm{d}R_{pc}\left(X, \Delta, \theta_c, r_p\right) \quad (20)$$

where

$$\tilde{\alpha}_0\left(X, \theta_c, r_p\right) = R\left(X, \theta_c, r_p\right) - R\left(X, \theta_c, r_c\right) \quad (21)$$

is the residual range curvature term, and

$$\mathrm{d}R_{pc}\left(X, \Delta, \theta_c, r_p\right) = \mathrm{d}R\left(X, \Delta, \theta_c, r_p\right) - \mathrm{d}R\left(X, \Delta, \theta_c, r_c\right) \quad (22)$$

is the range-dependent NsRCM term. One can see that range-dependent motion errors can be removed by precise interpolation along range direction in the range-compressed domain.

The RC-MOCO is similar to the one-step MOCO (OS-MOCO) algorithm [43], [44], [45]. However, the traditional OS-MOCO algorithm is derived for stripmap mode, and spotlight mode has some differences. For clarity, the motion error geometric models about stripmap and spotlight modes are shown in Fig. 2.

For stripmap SAR imaging, the line of sight (LOS) direction is fixed and always parallel to the direction of the scene center line. As the platform moves, the unirradiated targets enter the beam while the targets inside the beam gradually move out of the beam. Usually, range-dependent motion errors are compensated along the scene center line. As a result, the fixed LOS direction means that the instantaneous range of the targets at the scene center line coincides with range-dependent motion errors along the LOS direction. For the ith range-compressed signal, the pseudocode of the OS-MOCO algorithm for the ith pulse is given by

$$S_0'\left(X_i, \Delta, \vartheta, r\right) = \quad (23a)$$

$$\text{interp}\left[R_n + \mathrm{d}R_{pc}\left(X_i, \Delta, \theta_c, r\right), S_{02}\left(X_i, \Delta, \vartheta, r\right), R_n\right]$$

$$S_0\left(X_i, \Delta, \vartheta, r\right) = S_0'\left(X_i, \Delta, \vartheta, r\right) \cdot H_3\left(X_i, \Delta, \theta_c, r\right) \quad (23b)$$

where, R_n is the range axis for range compressed signal.

However, the direction of LOS is a time-variant for spotlight mode, whereas the direction of the scene center line is fixed. The inconsistency between LOS and the scene center line causes the mismatch between target range and range-dependent motion errors. As a result, extra range cell rearrangement is needed before phase errors compensation. The pseudocode of the new RC-MOCO is given by

$$S_2' = \text{interp1}\left[R_n, S_2\left(X_i, \Delta, \vartheta, r\right), R\left(X_i, \Delta, \theta_c, r\right)\right] \quad (24a)$$

$$S_2' = \text{interp1}\left[R\left(X_i, \theta_c, r\right) + \mathrm{d}R_{pc}\left(X_i, \Delta, \theta_c, r\right), \ldots\right.$$
$$\left.S_2'\left(X_i, \Delta, \vartheta, r\right), R\left(X_i, \theta_c, r\right)\right] \quad (24b)$$

$$S_2'\left(X_i, \Delta, \vartheta, r\right) = S_2'\left(X_i, \Delta, \vartheta, r\right) \cdot H_3\left(X_i, \Delta, \theta_c, r\right) \quad (24c)$$

$$S_2\left(X_i, \Delta, \vartheta, r\right) = \text{interp1}\left[R\left(X_i, \theta_c, r\right), S_2', R_n\right] \quad (24d)$$

where, $H_3(X_i, \Delta, r)$ is the phase compensation function corresponding to the slant range error, i.e,

$$H_3\left(X_i, \Delta, \theta_c, r\right) = \exp\left[jk_{rc} \cdot \mathrm{d}R_{pc}\left(X, \Delta, \theta_c, r\right)\right]. \quad (25)$$

B. Residual RCC

After compensating for range-dependent motion errors, the residual range curvature becomes the main obstacle on RCMC. As shown in (20), the residual range curvature exists in the zero-order term $\tilde{\alpha}_0(X, \theta_c, r_p)$. We perform a Taylor expansion on it and retain its second-order term

$$\tilde{\alpha}_0\left(X, \theta_c, r_p\right) = R\left(X, \theta_c, r_p\right) - R\left(X, \theta_c, r_c\right)$$
$$\approx \Delta r_{pc} - \frac{\cos^2\theta_c}{2} \cdot \frac{\Delta r_{pc}}{r_p \cdot r_c} \cdot X^2. \quad (26)$$

We can see that the first term is a constant range difference, and it does not produce range cell migration. The second term is the range curvature term, which is range-dependent. To simplify expression and avoid misunderstanding, we simplify $\alpha_0(X, \Delta, \theta_c, r_p)$ as α_0, and simplify $\tilde{\alpha}_0(X, \theta_c, r_p)$ as $\tilde{\alpha}_0$. In practice, the condition $\Delta r_{pc} \ll r_c$ can be always met. As a result, the range curvature can be given by

$$\mathrm{RC}\left(X, \theta_c, r_p\right) \approx -\frac{\cos^2\theta_c}{2} \cdot \frac{\Delta r_{pc}}{r_c^2} \cdot X^2. \quad (27)$$

In order to verify the rationality of this hypothesis, the range curvature approximation error curves with different Δr_{pc} are shown in Fig. 3, respectively. The simulation reference range is 20 km, the squint angle is 20°, and the synthetic aperture length is about 1.13 km. In practice, the Δr_{pc} is generally between 100 m and 3 km, limited by the maximum operating range of airborne SAR systems. From Fig. 3, one can see that (27) is precise enough to be suitable for high-resolution and widefield SAR imaging.

Based on this, the precise range wavenumber domain signal $S_2(k_r, X, \Delta, \vartheta_p)$ after KTA processing can be expressed as

$$S_2\left(k_r, X, \Delta, \vartheta_p\right) = \exp\left(-jk_r\Delta r_{pc}\right)\exp\left(-jk_{rc}\alpha_1\vartheta_p\right)$$
$$\cdot \exp\left(-j\frac{k_{rc}^2}{k_r + k_{rc}} \cdot \frac{\cos^2\theta_c}{2r_c^2} \cdot \Delta r_{pc} \cdot X^2\right) \quad (28)$$

where, α_1 donates $\alpha_1(X, \Delta, \theta_c, r_p)$. The first exponent term is the range difference, determined by the target range. The second

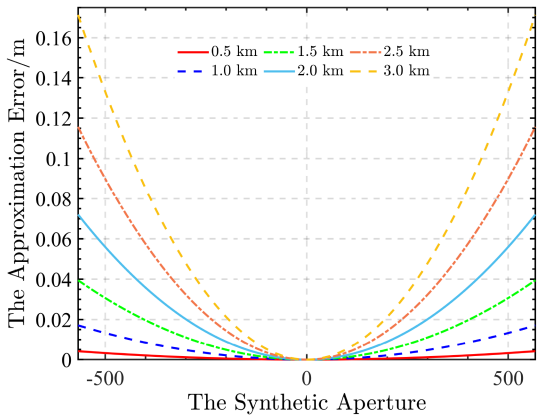

Fig. 3. Range curvature approximation error curves with different Δr_{pc}.

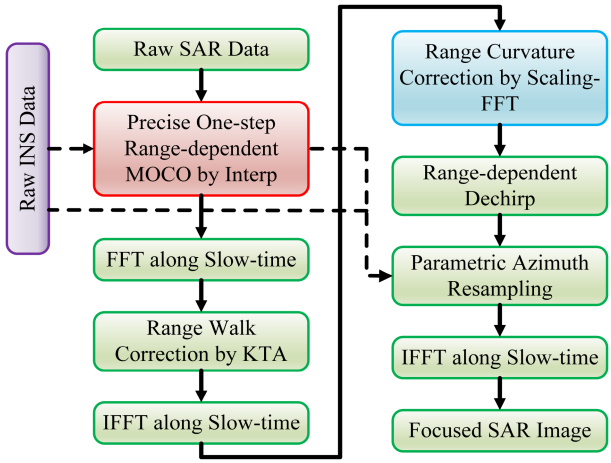

Fig. 4. Proposed algorithm's flowchart.

exponent term is the linear phase term involving the targets' azimuth angle, which decides the azimuth position of the targets. The third exponent term is the range curvature term, and we will introduce a new algorithm to correct it. First, the range curvature term is rewritten as

$$S_{\mathrm{RC}}\left(k_r, X, \theta_{\mathrm{c}}, r_{\mathrm{p}}\right) = \exp\left(-j\frac{k_{\mathrm{rc}}^2}{k_{\mathrm{r}}+k_{\mathrm{rc}}}\cdot\frac{\cos^2\theta_{\mathrm{c}}}{2r_{\mathrm{c}}^2}\cdot\Delta r_{\mathrm{pc}}\cdot X^2\right). \tag{29}$$

In practice, the SAR echo signal can always be regarded as a narrow band signal, and the swath width is often much smaller than the reference range. In other words, the following inequality holds:

$$\frac{\Delta r_{\mathrm{pc}}}{r_{\mathrm{c}}} \ll 1, \text{ and } \frac{k_{\mathrm{r}}}{k_{\mathrm{rc}}} \ll 1. \tag{30}$$

Based on these two hypotheses, the (29) can be approximated as

$$S_{\mathrm{RC}}\left(k_{\mathrm{r}}, X, \theta_{\mathrm{c}}, r_{\mathrm{p}}\right) \approx \exp\left[-j\left(k_{\mathrm{r}}-k_{\mathrm{rc}}\right)\cdot\frac{\cos^2\theta_{\mathrm{c}}}{2r_{\mathrm{c}}^2}\cdot\Delta r_{\mathrm{pc}}\cdot X^2\right]. \tag{31}$$

By combining (26), the (28) can be rewritten as

$$S_2\left(k_{\mathrm{r}}, X, \Delta, \vartheta_{\mathrm{p}}\right) = \exp\left[-jk_{\mathrm{rc}}\cdot\left(\tilde{\alpha}_0+\alpha_1\vartheta_{\mathrm{p}}\right)\right] \exp\left[-jk_{\mathrm{r}}\cdot\Delta r_{\mathrm{pc}}\left(1-\frac{\cos^2\theta_{\mathrm{c}}}{2r_{\mathrm{c}}^2}\cdot X^2\right)\right]. \tag{32}$$

Compared with (6), we can see that the direction of range curvature becomes opposite after KTA processing. Based on (32), we can correct range curvature by a resample operation along fast time after range inverse Fourier transform. However, the resample accuracy is constrained by the interpolation kernel length and computational complexity. We can see from (32) that the range-dependent range curvature already becomes a linear function of range difference Δr_{pc} after appropriate approximation. Therefore, the SFT [46], [47], [48] can be utilized to realize the RCC operation by a time-variant scaling factor $\gamma_r(X)$. It is clear that the $\gamma_r(X)$ can be expressed by

$$\gamma_r(X) = \frac{1}{1-\frac{\cos^2\theta_{\mathrm{c}}}{2r_{\mathrm{c}}^2}\cdot X^2}. \tag{33}$$

It is worth noting that the SFT dramatically improves the efficiency of RCC while maintaining high correction precision. After RCC, the precise signal expression is given by

$$\tilde{S}_2\left(X, \Delta, \vartheta_{\mathrm{p}}, r\right) = \mathrm{sinc}\left(r-\Delta r_{\mathrm{pc}}\right)\cdot\exp\left[-jk_{\mathrm{rc}}\left(\tilde{\alpha}_0+\alpha_1\vartheta_{\mathrm{p}}\right)\right] \tag{34}$$

and the reference function H_2 becomes

$$\tilde{H}_2\left(X, \Delta, r_{\mathrm{p}}\right) = \exp\left[jk_{\mathrm{rc}}\cdot\tilde{\alpha}_0\left(X, \theta_{\mathrm{c}}, r_{\mathrm{p}}\right)\right]. \tag{35}$$

After phase compensation by $\tilde{H}_2$, the (15) is now considered as the precise signal expression before azimuth focusing, i.e.,

$$\tilde{S}_3\left(X, \Delta, \vartheta_{\mathrm{p}}, r_{\mathrm{p}}\right) = S_3\left(X, \Delta, \vartheta_{\mathrm{p}}, r_{\mathrm{p}}\right). \tag{36}$$

After the parametric azimuth resampling, the well-focused image is given by

$$\tilde{I}\left(\vartheta, r\right) = \mathrm{IFFT}\left[\tilde{S}_3\left(X, \Delta, \vartheta_{\mathrm{p}}, r\right)\right] = \mathrm{sinc}\left(r-\Delta r_{\mathrm{pc}}\right)\cdot\mathrm{sinc}\left(\vartheta-\vartheta_{\mathrm{p}}\right). \tag{37}$$

For clarity, the block diagram of our proposed algorithm's is depicted in Fig. 4.

IV. Experiments and Analysis

This section presents the experiment results of simulated and real-measured SAR data via the developed algorithm. The performance of our proposed WPPFA is thoroughly investigated based on extensive comparison experiments.

A. Experiment With Simulated SAR Data

In this section, the results of simulated widefield spotlight SAR echo data, processed by our proposed algorithm, are introduced to illustrate the effectiveness of WPPFA. The SAR echo data are simulated with a point target scene, depicted in

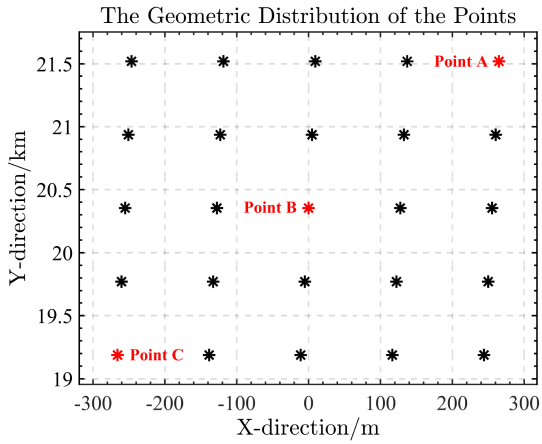

Fig. 5. Point target scenario.

TABLE I
PARAMETERS OF SIMULATION SAR SYSTEM

Parameter	Value	Parameter	Value
Carrier frequency	10 GHz	Pulse repeat frequency	500 Hz
Band width	810 MHz	Azimuth beam width	1.8°
Platform height	3194 m	Squint angle	20°
The center range	20.5 km	Platform velocity	69.27 m/s
The range samples	16384	The number of pulses	8192

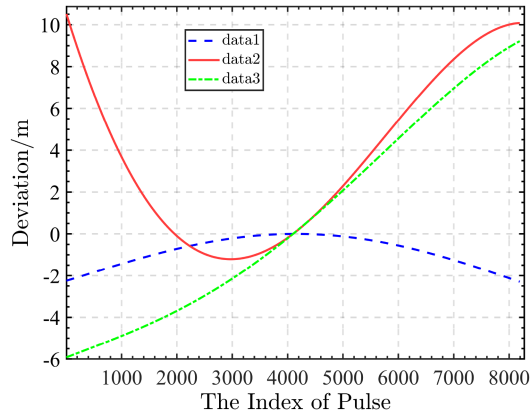

Fig. 6. Three-axis direction deviations.

Fig. 5. It can be seen that the point target scenario is composed of a five-by-five dot matrix. The size of this scenario is about 2330 m (Range) × 518 m (Azimuth).

Furthermore, a simulation SAR system working at X-band generates the SAR echo data. Some crucial radar system parameters are shown in Table I. According to these parameters, the nominal range resolution is 0.164 m, and the azimuth resolution is 0.239 m.

In addition, the trajectory deviations, derived from a real inertial navigation system (INS), are added into the simulated SAR echo to produce the spatial-variant motion errors. The trajectory deviations are depicted in Fig. 6. One can see that the trajectory deviations are severe, and the maximum deviations in the *X*-, *Y*-, and *Z*-directions are about –2.3, 10.5, and 9.2 m, respectively. Considering the width of scenario, the radar parameters and the severe trajectory deviations, the spatial-variant characteristics of the motion errors will not be neglected.

In this experiment, the scene center point B is selected as the imaging reference point. Our proposed WPPFA is utilized to image the simulated SAR echo. We also use PPFA and PFA to process the same SAR data to compare the superiority. The images produced by the three algorithms are shown in Fig. 7. We can see that our proposed algorithm achieves well-focused images of all the points. As reference point B, the edge points are also sharply focused. Their main-lobes have almost no spreading, and the distortion of the side-lobes is also acceptable. However, for the result of PPFA, one can see that the main-lobes in the range direction are significantly diffusing due to residual range curvature, especially for those edge points. PFA result shows that only reference point B is well-focused, whereas the other point targets are distinctly defocusing due to spatial-variant motion errors. Clearly, our proposed algorithm achieves the best imaging result, owing to the developed RC-MOCO and RCC approaches. For this reason, we will introduce the RCMC and azimuth-focused results to illustrate these improvements in the following deeply.

The RCMC results of the three different point targets, i.e., points A, B, and C in Fig. 7, obtained through the three algorithms are shown in Fig. 8(a)–(c). One can see that WPPFA achieves excellent RCMC results. Both reference point B and the edge points have straight envelopes, and the signal's energy is concentrated onto the same slant range cell. These results indicate that our proposed algorithm can completely remove NsRCM and correct residual range curvature precisely. However, for PPFA, the residual range curvature is visible, which is the leading cause of the undesired range cell migration. Moreover, the signal envelope spreads into multiple nearby range cells due to the combined impact of residual range curvature and motion errors. For PFA, range-dependent motion errors are the primary impediment to obtaining good RCMC results. As a result, the NsRCM is significant, and the signal envelope disperses into several neighboring range cells.

In addition, to illustrate the MOCO performance, we also present the profiles of different points' azimuth impulse response functions produced by the three algorithms in Fig. 9(a)–(c). One can see that our proposed algorithm achieves the best-focused results for all three points. The focused results of points A and C are comparable to that of reference point B, indicating the developed RC-MOCO and RCC enable WPPFA to achieve well-focused widefield SAR imaging with spatial-variant motion errors. However, the results of points A and C formed by PPFA and PFA are significant defocusing. On the one hand, NsRCM and range curvature shorten the effective synthetic aperture length resulting in the main-lobe widening. On the other hand, spatial-variant motion errors degrade the azimuth focusing, causing side-lobe distortion.

We also calculate the impulse response width (IRW), peak side-lobe ratio (PSLR), and integrated side-lobe ratio (ISLR) of these impulse response functions to assess the compensation performance of the three algorithms quantitatively. The IRW, PSLR, and ISLR are listed in Tables II, III, and IV, respectively. According to Table II, it can be seen that the IRWs of

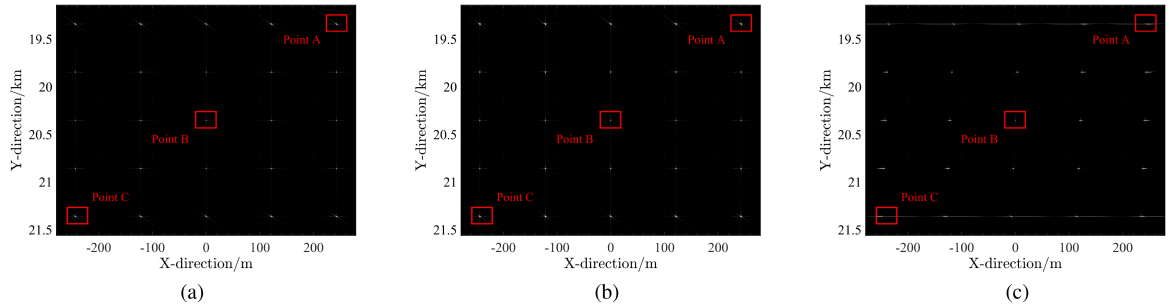

Fig. 7. Point target imaging results formated by different algorithms. (a) WPPFA. (b) PPFA. (c) PFA.

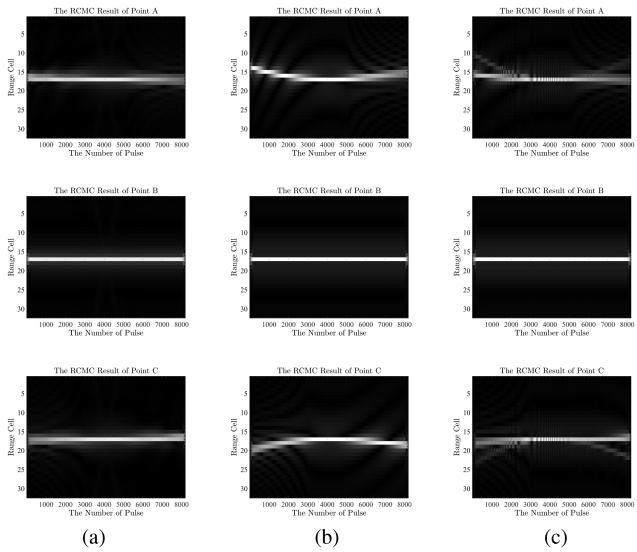

Fig. 8. RCMC results formated by different algorithms. (a) WPPFA. (b) PPFA. (c) PFA.

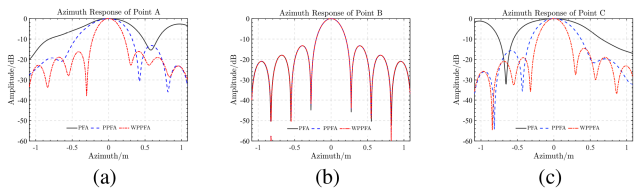

Fig. 9. Azimuth impulse response functions processed by different algorithms. (a) Azimuth response of point A. (b) Azimuth response of point B. (c) Azimuth response of point C.

TABLE II
IRW OF DIFFERENT POINTS PROCESSED BY ALL THE ALGORITHMS

Point \ Algorithm	WPPFA	PPFA	PFA
Point A (m)	0.2601	0.4518	0.5921
Point B (m)	0.2438	0.2438	0.2444
Point C (m)	0.2640	0.4051	0.7453

TABLE III
PSLR OF DIFFERENT POINTS PROCESSED BY ALL THE ALGORITHMS

Point \ algorithm	WPPFA	PPFA	PFA
Point A (dB)	−16.0620	−13.1708	−2.6638
Point B (dB)	−13.2694	−13.2693	−13.2787
Point C (dB)	−14.5375	−15.6606	−1.2218

TABLE IV
ISLR OF DIFFERENT POINTS PROCESSED BY ALL THE ALGORITHMS

Point \ algorithm	WPPFA	PPFA	PFA
Point A (dB)	−12.1842	−15.2300	3.2456
Point B (dB)	−10.1921	−10.1921	−10.2281
Point C (dB)	−13.2953	−16.4727	1.7646

TABLE V
PARAMETERS OF REAL SAR SYSTEM

Parameter	Value	Parameter	Value
Carrier frequency	9.6 GHz	Pulse repeat frequency	533 Hz
Band width	480 MHz	Azimuth beam width	2.3 deg
Platform height	7534 m	Squint angle	0.25 deg
The center range	24.4 km	Platform velocity	154 m/s
The range samples	16384	The number of pulses	8192

the WPPFA are almost the same as the simulation azimuthal resolution, which means the three points are all well-focused. However, the other algorithms have some degree of defocusing. In Tables III and IV, WPPFA maintains the lowest level of the PSLR and ISLR than other algorithms, indicating that the proposed WPPFA algorithm achieves excellent widefield SAR imaging results.

B. Experiment With Real-Measured SAR Data

In this section, we will apply our proposed algorithm to real-measured widefield SAR echo data, and the experiment results are introduced to investigate the WPPFA's imaging performance. This SAR data are recorded by an airborne SAR system mounted on an unmanned aerial vehicle. Some key radar system parameters are listed in the Table. V. According to these parameters,

(a) (b) (c)

Fig. 10. Full-image results formated by different algorithms. (a) WPPFA. (b) PPFA. (c) PFA.

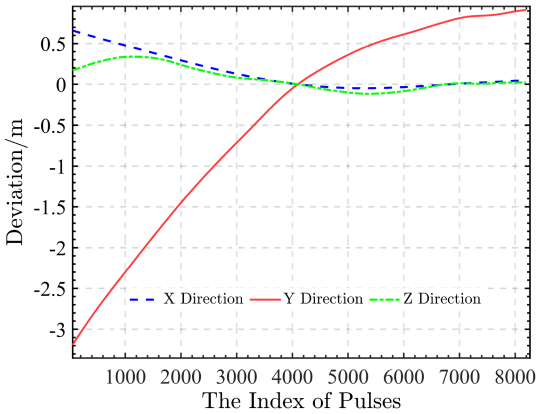

Fig. 11. Three-axis motion errors in real-measured SAR data.

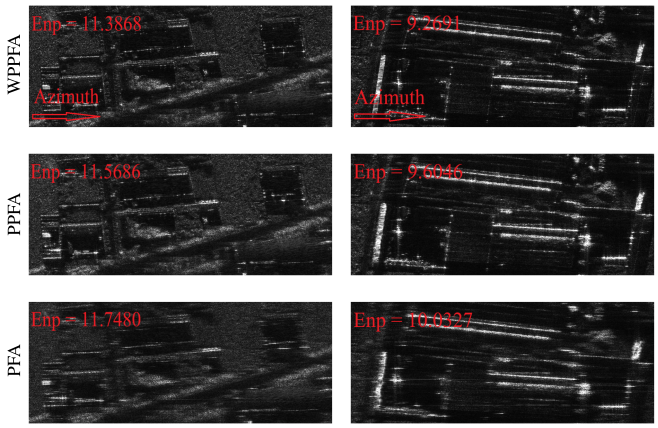

(a) (b)

Fig. 12. RCMC results formated by different algorithms. (a) Scene A. (b) Scene B.

the system achieves a range resolution of about 0.27 m with a 480 MHz signal bandwidth and an azimuth resolution of roughly 0.16 m with a synthetic aperture of about 2.37 km. It can be considered a high-resolution and widefield SAR system due to a swath width of about 4.48 km.

The trajectory deviations are depicted in Fig. 11. The raw trajectory deviation data are collected by an INS mounted on the platform. One can see that the deviation along the vertical track direction is serious, which reaches about –3.2 m in the *Y*-direction, indicating that the range-dependent characteristic of motion errors cannot be ignored.

The proposed WPPFA algorithm is used to process the SAR echo data to achieve high-resolution and widefield SAR imaging. Then, PPFA and PFA are also used to image the same SAR echo. The images formed by the three algorithms are exhibited in Fig. 10. Fig. 10(a) shows that the image achieved by our proposed algorithm is focused with high quality. One can note the roads, villages, and wild scenes are clearly distinguished and well-focused with high contrast. However, the result processed by PPFA has some degree of defocusing, primarily in the scene edge. Furthermore, we can see that the result processed by PFA is seriously blurred and distorted in geometry due to range-dependent motion errors, particularly in the near-and far-range regions.

For the sake of clarity, the local scenes, highlighted in Fig. 10 by rectangles, are amplified in Fig. 12. We can see from Fig. 12 that our proposed WPPFA produces the best-focused results. The image contrast is high, and the edges of buildings and roads are

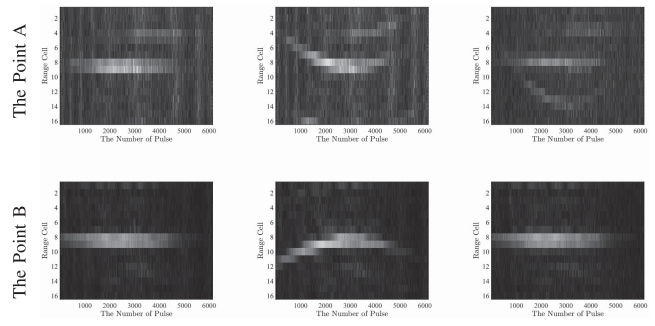

(a) (b) (c)

Fig. 13. RCMC results formated by different algorithms. (a) WPPFA. (b) PPFA. (c) PFA.

visible. However, the results of PPFA show that the side-lobe levels are higher in the range direction, and the main-lobes of dominant points are significantly widening. Moreover, the results formed by PFA are noticeably defocusing. Besides, from the entropy values marked in the upper left corner of these images, we can also notice that our proposed WPPFA achieves the best imaging results.

The RCMC results of two isolated point-like targets, A and B, processed by different algorithms, are displayed in Fig. 13. Fig. 13(a) shows that envelopes of signals processed by WPPFA are straight and smooth, meaning that the developed RC-MOCO

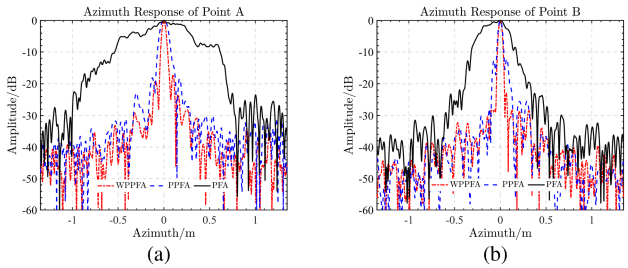

Fig. 14. Azimuth impulse response functions processed by different algorithms.

and RCC algorithms entirely remove NsRCM and residual range curvature. However, the residual range curvature severely affects PPFA's RCMC results. One can see that the signal's envelope spreads into multiple nearby range cells. Furthermore, the results of PFA are similar to that of WPPFA. But, compared to WPPFA, the range side-lobes are more prominent, indicating that the minor high-order NsRCM remains.

Furthermore, these two targets' azimuth impulse response functions are enlarged in Fig. 14. We can see that WPPFA indeed achieves better-focused results than other algorithms, as evidenced by narrower main-lobes and lower side-lobes. However, the resolution of PPFA's results is obviously degraded because the residual range curvature shortens the effective synthetic aperture length. The PFA's results are significantly defocused because the spatial-variant motion errors substantially impact the scene edge points.

V. Conclusion

This article develops a novel PPFA for high-resolution and widefield spotlight SAR imaging. First, the precise RC-MOCO approach is introduced, and the distinctions between RC-MOCO and OS-MOCO are thoroughly investigated. Based on this, an interpolation-based approach is presented to compensate precisely for the range-dependent motion errors. Following, the residual range curvature after range walk correction is derived, and a high-efficiency RCC is implemented using the SFT with the specific parameter. Finally, based on the above improvements, the azimuth-dependent phase errors are uniformly adjusted via parametric interpolation along the azimuth angle wavenumber axis. Finally, extensive simulated and real-measured SAR data experiments validate the proposal's superiority.

Acknowledgment

The authors would like to thank the anonymous reviewers for their valuable comments to improve the quality of this article.

References

[1] M. Zink et al., "TanDEM-X: 10 years of formation flying bistatic SAR interferometry," *IEEE J. Sel. Topics Appl. Earth Observ. Remote Sens.*, vol. 14, pp. 3546–3565, 2021, doi: 10.1109/JSTARS.2021.3062286.

[2] J. Xia, N. Yokoya, B. Adriano, L. Zhang, G. Li, and Z. Wang, "A benchmark high-resolution GaoFen-3 SAR dataset for building semantic segmentation," *IEEE J. Sel. Topics Appl. Earth Observ. Remote Sens.*, vol. 14, pp. 5950–5963, 2021, doi: 10.1109/JSTARS.2021.3085122.

[3] B. Pyne, H. Saito, P. R. Akbar, J. Hirokawa, T. Tomura, and K. Tanaka, "Development and performance evaluation of small SAR system for 100-kg class satellite," *IEEE J. Sel. Topics Appl. Earth Observ. Remote Sens.*, vol. 13, pp. 3879–3891, 2020, doi: 10.1109/JSTARS.2020.3006396.

[4] S. V. Baumgartner and G. Krieger, "Simultaneous high-resolution wide-field SAR imaging and ground moving target indication: Processing approaches and system concepts," *IEEE J. Sel. Topics Appl. Earth Observ. Remote Sens.*, vol. 8, no. 11, pp. 5015–5029, Nov. 2015, doi: 10.1109/JSTARS.2015.2450019.

[5] A. Cristea, A. M. Johansson, A. P. Doulgeris, and C. Brekke, "Automatic detection of low-backscatter targets in the arctic using wide swath Sentinel-1 imagery," *IEEE J. Sel. Topics Appl. Earth Observ. Remote Sens.*, vol. 15, pp. 8870–8883, 2022, doi: 10.1109/JSTARS.2022.3214069.

[6] M. AlShaya, M. Yaghoobi, and B. Mulgrew, "Ultrahigh resolution wide swath MIMO-SAR," *IEEE J. Sel. Topics Appl. Earth Observ. Remote Sens.*, vol. 13, pp. 5358–5368, 2020, doi: 10.1109/JSTARS.2020.3021914.

[7] J. Wei, Y. Li, R. Yang, L. Li, and L. Guo, "Method of high signal-to-noise ratio and wide swath SAR imaging based on continuous pulse coding," *IEEE J. Sel. Topics Appl. Earth Observ. Remote Sens.*, vol. 15, pp. 2185–2196, 2022, doi: 10.1109/JSTARS.2022.3153118.

[8] M. D. Desai and W. K. Jenkins, "Convolution backprojection image reconstruction for spotlight mode synthetic aperture radar," *IEEE Trans. Image Process.*, vol. 1, no. 4, pp. 505–517, Oct. 1992, doi: 10.1109/83.199920.

[9] J. Ding, Y. Wu, and H. Zhang, "A fast BP algorithm for bistatic spotlight SAR based on spectrum compression," in *Proc. 6th Asia-Pacific Conf. Synthetic Aperture Radar*, Xiamen, China, 2019, pp. 1–5, doi: 10.1109/APSAR46974.2019.9048432.

[10] L. Zhang, H.-L. Li, Z.-J. Qiao, and Z.-W. Xu, "A fast BP algorithm with wavenumber spectrum fusion for high-resolution spotlight SAR imaging," *IEEE Geosci. Remote Sens. Lett.*, vol. 11, no. 9, pp. 1460–1464, Sep. 2014, doi: 10.1109/LGRS.2013.2295326.

[11] J. Wu, Y. Li, W. Pu, Z. Li, and J. Yang, "An effective autofocus method for fast factorized back-projection," *IEEE Trans. Geosci. Remote Sens.*, vol. 57, no. 8, pp. 6145–6154, Aug. 2019, doi: 10.1109/TGRS.2019.2904608.

[12] M. Bao, S. Zhou, L. Yang, M. Xing, and L. Zhao, "Data-driven motion compensation for airborne bistatic SAR imagery under fast factorized back projection framework," *IEEE J. Sel. Topics Appl. Earth Observ. Remote Sens.*, vol. 14, pp. 1728–1740, 2021, doi: 10.1109/JSTARS.2020.3002394.

[13] L. Ran, Z. Liu, T. Li, R. Xie, and L. Zhang, "An adaptive fast factorized back-projection algorithm with integrated target detection technique for high-resolution and high-squint spotlight SAR imagery," *IEEE J. Sel. Topics Appl. Earth Observ. Remote Sens.*, vol. 11, no. 1, pp. 171–183, Jan. 2018, doi: 10.1109/JSTARS.2017.2771503.

[14] Q. Chen et al., "A Fast Cartesian back-projection algorithm based on ground surface grid for GEO SAR focusing," *IEEE Trans. Geosci. Remote Sens.*, vol. 60, 2022, Art no. 5217114, doi: 10.1109/TGRS.2021.3125797.

[15] Y. Luo, F. Zhao, N. Li, and H. Zhang, "A modified Cartesian factorized back-projection algorithm for highly squint spotlight synthetic aperture radar imaging," *IEEE Geosci. Remote Sens. Lett.*, vol. 16, no. 6, pp. 902–906, Jun. 2019, doi: 10.1109/LGRS.2018.2885196.

[16] Q. Dong, Z. Yang, G. Sun, and M. Xing, "Cartesian factorized back-projection algorithm for synthetic aperture radar," in *Proc. IEEE Int. Geosci. Remote Sens. Symp.*, Beijing, China, 2016, pp. 1074–1077, doi: 10.1109/IGARSS.2016.7729272.

[17] R. Bamler, "A comparison of range-Doppler and wavenumber domain SAR focusing algorithms," *IEEE Trans. Geosci. Remote Sens.*, vol. 30, no. 4, pp. 706–713, Jul. 1992, doi: 10.1109/36.158864.

[18] X. Tan et al., "An efficient range-Doppler domain ISAR imaging approach for rapidly spinning targets," *IEEE Trans. Geosci. Remote Sens.*, vol. 58, no. 4, pp. 2670–2681, Apr. 2020, doi: 10.1109/TGRS.2019.2953303.

[19] W. Fan, M. Zhang, J. Li, and P. Wei, "Modified range-Doppler algorithm for high squint SAR echo processing," *IEEE Geosci. Remote Sens. Lett.*, vol. 16, no. 3, pp. 422–426, Mar. 2019, doi: 10.1109/LGRS.2018.2873680.

[20] C. Li et al., "Focusing the L-band spaceborne bistatic SAR mission data using a modified RD algorithm," *IEEE Trans. Geosci. Remote Sens.*, vol. 58, no. 1, pp. 294–306, Jan. 2020, doi: 10.1109/TGRS.2019.2936255.

[21] Y. Wang, J. Li, F. Xu, and J. Yang, "A new nonlinear chirp scaling algorithm for high-squint high-resolution SAR imaging," *IEEE Geosci. Remote Sens. Lett.*, vol. 14, no. 12, pp. 2225–2229, Dec. 2017, doi: 10.1109/LGRS.2017.2758386.

[22] P. -C. Chen and J. -F. Kiang, "Chirp scaling algorithms for SAR imaging under high squint angles," in *Proc. IEEE Int. Symp. Antennas Propag. USNC/URSI Nat. Radio Sci. Meeting*, San Diego, CA, USA, 2017, pp. 203–204, doi: 10.1109/APUSNCURSINRSM.2017.8072144.

[23] L. Gao-gao, Z. Lin-rang, L. Nan, C. Guang-feng, and Z. Yan, "Focusing highly squinted data using the extended nonlinear chirp scaling algorithm," *IEEE Geosci. Remote Sens. Lett.*, vol. 10, no. 2, pp. 342–346, Mar. 2013, doi: 10.1109/LGRS.2012.2203785.

[24] J. Wang, T. Zhang, M. Yuan, and Y. Li, "A modified nonlinear chirp scaling algorithm for highly squinted SAR on maneuvering platform," in *Proc. IGARSS IEEE Int. Geosci. Remote Sens. Symp.*, Kuala Lumpur, Malaysia, 2022, pp. 2035–2038, doi: 10.1109/IGARSS46834.2022.9884737.

[25] Y. Wu, H. Song, X. Shang, and J. Zheng, "Improved RMA based on nonuniform fast Fourier Transforms (NUFFT's)," in *Proc. 9th Int. Conf. Signal Process.*, Beijing, 2008, pp. 2489–2492, doi: 10.1109/ICOSP.2008.4697654.

[26] X. Mao, X. He, and D. Li, "Knowledge-aided 2-D autofocus for spotlight SAR range migration algorithm imagery," *IEEE Trans. Geosci. Remote Sens.*, vol. 56, no. 9, pp. 5458–5470, Sep. 2018, doi: 10.1109/TGRS.2018.2817507.

[27] J. Yang, G. -C. Sun, J. Chen, Y. Wu, and M. Xing, "A subaperture imaging scheme for wide azimuth beam airborne SAR based on modified RMA with motion compensation," in *Proc. IEEE Geosci. Remote Sens. Symp.*, Quebec City, QC, Canada, 2014, pp. 608–611, doi: 10.1109/IGARSS.2014.6946496.

[28] A. Daoxiang, H. Xiaotao, and Z. Zhimin, "Two-step motion compensation of range migration algorithm for airborne spotlight SAR imaging," in *Proc. 2nd Asian-Pacific Conf. Synthetic Aperture Radar*, Xi'an, China, 2009, pp. 350–353, doi: 10.1109/APSAR.2009.5374165.

[29] J. Chen, J. Zhang, Y. Jin, H. Yu, B. Liang, and D.-G. Yang, "Real-time processing of spaceborne SAR data with nonlinear trajectory based on variable PRF," *IEEE Trans. Geosci. Remote Sens.*, vol. 60, 2022, Art no. 5205212, doi: 10.1109/TGRS.2021.3067945.

[30] J. Li, P. Wang, J. Chen, J. Wang, and W. Yang, "An improved two-step motion compensation method based on raw data," in *Proc. IEEE Int. Geosci. Remote Sens. Symp.*, Milan, Italy, 2015, pp. 4484–4486, doi: 10.1109/IGARSS.2015.7326823.

[31] Y. Tang, M. -D. Xing, and Z. Bao, "The polar format imaging algorithm based on double chirp-Z transforms," *IEEE Geosci. Remote Sens. Lett.*, vol. 5, no. 4, pp. 610–614, Oct. 2008, doi: 10.1109/LGRS.2008.2000971.

[32] J. Chen, D. An, W. Wang, Y. Luo, L. Chen, and Z. Zhou, "Extended polar format algorithm for large-scene high-resolution WAS-SAR imaging," *IEEE J. Sel. Topics Appl. Earth Observ. Remote Sens.*, vol. 14, pp. 5326–5338, 2021, doi: 10.1109/JSTARS.2021.3081515.

[33] X. Nie, W. Lei, and L. Zhuang, "A two-step wide-scene polar format algorithm for high-resolution highly-squinted SAR," *IEEE Geosci. Remote Sens. Lett.*, vol. 19, 2022, Art no. 4503405, doi: 10.1109/LGRS.2022.3140865.

[34] F. Wang, L. Zhang, Y. Cao, and G. Wang, "Integrating motion compensation with polar format interpolation for enhanced highly squinted airborne SAR imagery," *IEEE Access*, vol. 7, pp. 177101–177113, 2019, doi: 10.1109/ACCESS.2019.2946190.

[35] F. Wang, L. Zhang, Y. Cao, T.-S. Yeo, and G. Wang, "A novel algorithm for hypersonic SAR imaging with large squint angle and dive trajectory," *IEEE Geosci. Remote Sens. Lett.*, vol. 19, 2022, Art no. 4016105, doi: 10.1109/LGRS.2021.3099809.

[36] Z. Meng, L. Zhang, Y. Ma, G. Wang, and H. Jiang, "Accelerating minimum entropy autofocus with stochastic gradient for UAV SAR imagery," *IEEE Geosci. Remote Sens. Lett.*, vol. 19, 2022, Art. no. 4017805, doi: 10.1109/LGRS.2021.3106636.

[37] J. Chen and H. Yu, "Wide-beam SAR autofocus based on blind resampling," *Sci. China Inf. Sci.*, vol. 66, 2023, Art. no. 140304.

[38] L. Yang, Y. Liao, L. Zhang, and M.-D. Xing, "Motion compensation in post-PFA domain for high resolution spotlight SAR imagery," in *Proc. IEEE CIE Int. Conf. Radar*, Chengdu, 2011, pp. 376–379, doi: 10.1109/CIE-Radar.2011.6159556.

[39] X. Mao, D. Zhu, and Z. Zhu, "Polar format algorithm wavefront curvature compensation under arbitrary radar flight path," *IEEE Geosci. Remote Sens. Lett.*, vol. 9, no. 3, pp. 526–530, May 2012, doi: 10.1109/LGRS.2011.2173291.

[40] Y. Miao, J. Wu, Z. Li, and J. Yang, "A generalized wavefront-curvature-corrected polar format algorithm to focus bistatic SAR under complicated flight paths," *IEEE J. Sel. Topics Appl. Earth Observ. Remote Sens.*, vol. 13, pp. 3757–3771, 2020, doi: 10.1109/JSTARS.2020.2999966.

[41] N. E. Doren, "Space-variant post-filtering for wavefront curvature correction in polar-formatted spotlight-mode SAR imagery," Ph.D. dissertation, Univ. New Mexico, Albuquerque, NM, USA, 1999, doi: 10.2172/14165.

[42] L. Yang, M. Xing, Y. Wang, L. Zhang, and Z. Bao, "Compensation for the NsRCM and phase error after polar format resampling for airborne spotlight SAR raw data of high resolution," *IEEE Geosci. Remote Sens. Lett.*, vol. 10, no. 1, pp. 165–169, Jan. 2013, doi: 10.1109/LGRS.2012.2196676.

[43] D. Meng, D. Hu, and C. Ding, "A new approach to airborne high resolution SAR motion compensation for large trajectory deviations," *Chin. J. Electron.*, vol. 21, no. 4, pp. 764–769, Oct. 2012, doi: 10.1016/j.mee.2012.07.073.

[44] A. Ribalta, "One-step motion compensation algorithm for squinted SAR," in *Proc. IEEE Int. Geosci. Remote Sens. Symp.*, Beijing, China, 2016, pp. 1154–1157, doi: 10.1109/IGARSS.2016.7729292.

[45] M. Yang, D. Zhu, and W. Song, "Comparison of two-step and one-step motion compensation algorithms for airborne synthetic aperture radar," *Electron. Lett.*, vol. 51, no. 14, pp. 1108–1110, Jul. 2015, doi: 10.1049/el.2015.1350.

[46] O. ÇUlha and Y. Tanik, "Low complexity keystone transform and radon Fourier transform utilizing chirp-z transform," *IEEE Access*, vol. 8, pp. 105535–105541, 2020, doi: 10.1109/ACCESS.2020.3000998.

[47] J. Zheng, T. Su, W. Zhu, X. He, and Q. H. Liu, "Radar high-speed target detection based on the scaled inverse Fourier transform," *IEEE J. Sel. Topics Appl. Earth Observ. Remote Sens.*, vol. 8, no. 3, pp. 1108–1119, Mar. 2015, doi: 10.1109/JSTARS.2014.2368174.

[48] D. Zhu, Y. Li, and Z. Zhu, "A keystone transform without interpolation for SAR ground moving-target imaging," *IEEE Geosci. Remote Sens. Lett.*, vol. 4, no. 1, pp. 18–22, Jan. 2007, doi: 10.1109/LGRS.2006.882147.

Zhichao Meng was born in Shannxi Province, China, 1997. He received the B.S. and M.S. degrees in electronic engineering from Xidian University, Xian, China, in 2018 and 2021, respectively. He is currently working toward the Ph.D. degree in signal processing with the School of Electronics and Communication Engineering, Sun Yat-sen University, Guangzhou, China.

His research focuses on radar imaging.

Lei Zhang (Member, IEEE) was born in Zhejiang, China, in 1984. He received the Ph.D. degree in electronic engineering from Xidian University, Xi'an, China, in 2011.

He is currently a Professor with the School of Electronics and Communication Engineering, Sun Yat-sen University, Guangzhou, China. His research interests include radar imaging (synthetic aperture radar (SAR)/inverse SAR) and motion compensation.

Lili Chen was born in Guangxi, China, in 1982. She received the Ph.D. degree in computer science and technology from the National University of Defense Technology, Changsha, China, in 2011.

She is currently a Research Associate with Artificial Intelligence Research Center, National Innovation Institute of Defense Technology, Beijing, China. Her research interests include SAR imagery interpretation, artificial intelligence technology, and computer architecture.